Vortex Dissipation in Superfluid Third Sound Flows

by

Anand Swaminathan
Class of 2009

A thesis submitted to the
faculty of Wesleyan University
in partial fulfillment of the requirements for the
Degree of Bachelor of Arts
with Departmental Honors in Physics

Abstract:

This thesis probes possible mechanisms behind anomalous freedecays commonly observed in superfluid helium third sound flows. Several models, based on vortex dissipation, for the additional dissipation these anomalous freedecays imply are constructed, tested, and modified to be consistent with the observed characteristics. This work concludes that these simple models involving only vortex friction and a creation energy are insufficient to explain the observed characteristics. From this conclusion a model is proposed that holds promise for future study.

Acknowledgements:

I would like to heartily thank Professor Fred Ellis for his expert and tireless support and guidance throughout this project. Without him this work would not have been possible.

I would also like to extend my gratitude to the Wesleyan University Physics Department whose instruction provided me with the knowledge and resources that underpin this project and my development as a student of physics.

Contents

Chapter 1

Introduction

1.1 Overview

This thesis will attempt to explain aspects of third sound data previously taken by the Quantum Fluids Group at Wesleyan University. It seeks to further the understanding of and propose models for anomalous features observed in freedecays of third sound flows.

Format:

1. Chapter 1 will provide a brief introduction to the underlying physics of superfluidity and quantized vortices, examples of anomalous freedecays, and an analysis of the experimental parameters of the freedecays.

2. Chapter 2 will propose several possible vortex dissipation-based models for the observed anomalous phenomena and test their validity versus the experimental data. It will also find the number of vortices involved in the

dissipative motion.

3. Chapter 3 will find the positioning of the dissipating vortices within the cell.

4. Chapter 4 will propose a new model for the freedecay anomalies that is informed by the preceding work and holds promise for future work.

1.2 Superfluid

As the temperature of Helium-4 lowers below the λ-point, 2.17 K, the helium atoms collapse into a shared macroscopic quantum mechanical state and the fluid enters a new matter state, that of the superfluid. Because the conformity of the helium atoms to their shared quantum mechanical state dominates their normal inter-atomic interactions, superfluids allow experimentation on macroscopic quantum mechanical states. Below the λ-point, while the fluid itself does not separate, the fluid may now be modeled as being comprised of two interpenetrating, co-existing fluids. These fluids of the so-called "two-fluid model" exist simply for the purpose of conceptualizing the observed physical properties of the superfluid and do not in actuality exist as separate entities. One component, the normal fluid, is a soup of thermal excitations. The second component, the superfluid, has zero viscosity and infinite thermal conductivity. Each of these fluids can possess its own velocity at each point within the fluid and has its own mass density, a fractional component of the total mass density. Below 1 K, the temperatures at which the experiments for this work were performed, the liquid consists almost entirely of the superfluid component. [1]

1.3 Third Sound

A property of superfluid that is of particular importance to the work presented here is its ability to form uniformly adsorbed, very thin films upon all surfaces within a container. These films have the ability to propagate waves of several types through them. [1] In the wave motion of interest, third sound, the superfluid component moves in a largely lateral manner, sloshing back and forth like shallow water ocean waves. [1] As in shallow water waves, here too there is a restoring downward force, but it is the van der Waals force with the substrate, acting in the same capacity as the earth's gravitational force upon the ocean. In third sound waves, the normal fluid component of the film is clamped to the substrate via the dissipation of thermal excitations, that is its local velocity, $\mathbf{v}_n$, is zero everywhere within the film. The lateral displacement of the superfluid part far exceeds the vertical displacement and hence this largely horizontal motion allows the waves to be treated as a two-dimensional system. This is quite attractive as this condition removes the vertical dimension, greatly simplifying the fluid mechanics required.

1.4 Freedecays

A common experiment performed by the Quantum Fluids Group was to drive these waves up to a known amplitude and then to switch off the driving force and allow them to decay away. These waves should experience an exponential decay due to thermal fluctuations within the superfluid as it undergoes its oscillations. As is commonly known, on a semilogarithmic graph (logarithmic amplitude vs. linear time) exponentials are represented by straight lines. In fact, many of the

freedecays do exhibit this behavior as can be seen in Figure 1.1.

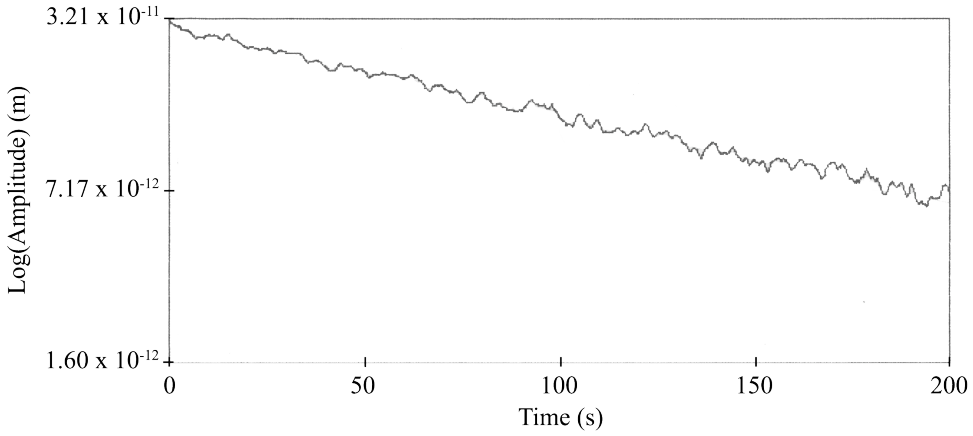

Figure 1.1: An example of a freedecay exhibiting normal, exponential linear behavior.

But, many of the freedecays, often taken at higher amplitudes, but not always, do not show this behavior. Instead, they display the characteristics of having two decay constants Q, one that is active only at high amplitudes which then transitions to another at low amplitudes, a "kink-like" transition, as in Figure 1.2. This behavior, with two straight lines on a semi-logarithmic plot, is quantitatively unexplained, but qualitative hypotheses have been proposed.

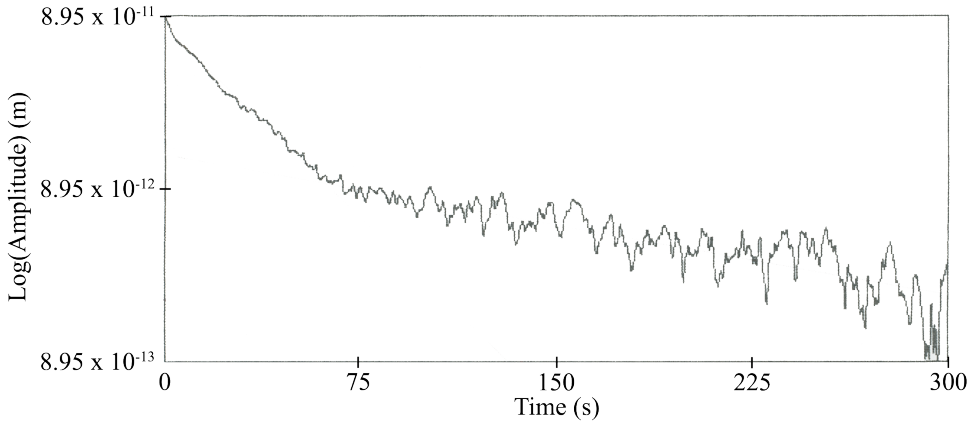

Figure 1.2: An example of a freedecay exhibiting the two decay constant "kink-like" behavior on a semi-logarithmic plot.

Some freedecays show an even stranger transition, a "bulge-like" curving transition from one decay constant to another as in Figure 1.3.

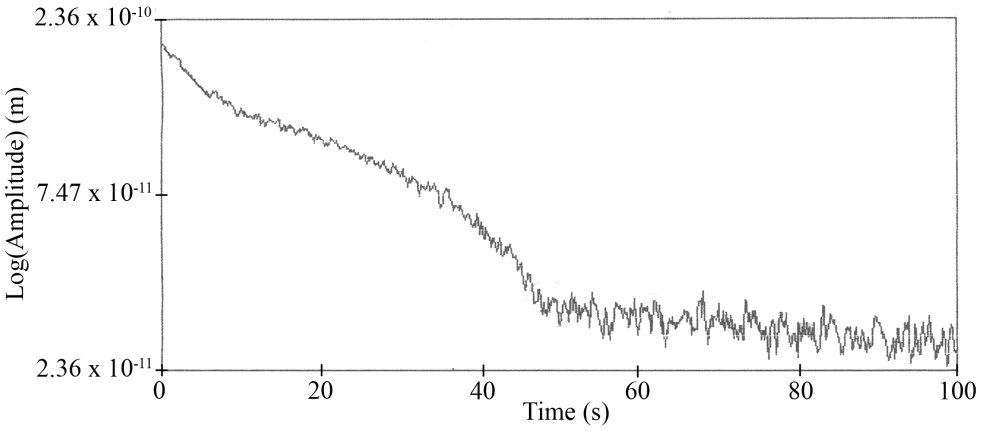

Figure 1.3: An example of a freedecay exhibiting the "bulge-like" transition behavior between decay constants on a semi-logarithmic plot.

The goal of this work will be to further understanding of and reach new con-

clusions about the mechanisms behind these anomalous freedecays, in particular those that exhibit the "bulge-like" transition behavior.

1.5 Superfluid Vortices

All vortices are characterized by a circular flow with closed streamlines around a core where quantitatively different behavior occurs. For superfluid vortices within ^{4}He, this core size is approximately $a_\circ = 1.3\,\text{Å}$. [2] What sets superfluid vortices apart from their cousins in non-superfluid is the fact that their circulations κ are quantized:

$$\kappa = \oint \mathbf{v}_s \cdot d\mathbf{l} = n\frac{h}{m_4}, \qquad \text{where } n = 0, 1, 2, \ldots \tag{1.1}$$

where $\mathbf{v}_s$ is the velocity of the superfluid, h is the Planck constant, and m_4 is the mass of a ^{4}He atom. What is notable here is the quantization condition indicated by the quantum number n. As can be seen from Equation 1.1 the velocity field of the vortex is also quantized:

$$v = n\frac{\hbar}{m_4 r}\hat{\phi} \tag{1.2}$$

where r is the distance from the center of the vortex. [3] The unit vector $\hat{\phi}$ denotes the direction of rotation, where positive ϕ denotes the right-handed rotation direction when looking on the vortices from above. This convention will be employed throughout the thesis.

While superfluid vortices are quantized, within our third sound films vortices with quantum numbers $n > 1$ are never seen, as single vortices of higher quantizations represent a higher energy state than a pair of singly-quantized vortices.

1.6 Magnus Force

Objects with circulation about them exposed to a flow experience a lateral force known as the Magnus force. Quantized superfluid vortices may be treated as physical objects due to their quantum stability and hence also undergo the Magnus force when placed in a third sound flow. [4] Due to the rotational flow of the vortex within the already existing (and locally uniform) fluid flow, the velocity of the fluid surrounding the vortex is faster than the background flow velocity on one side and slower than the background flow velocity on the other side. This imbalance of velocities results in a net force on the vortex due to the Bernoulli force as can be seen in Figure 1.4.

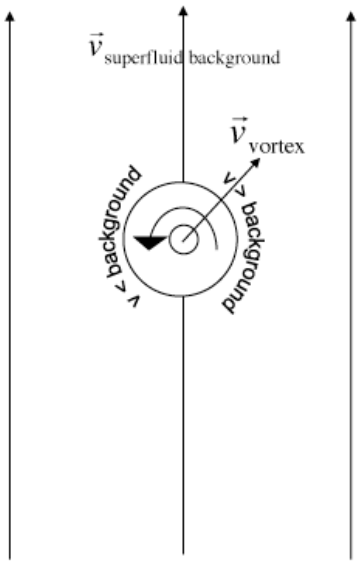

Figure 1.4: Illustration of the Magnus force upon a vortex.

The Magnus force in the case where the vortex is allowed to move at velocity

$\mathbf{v}_v$ is given by the following formula: [1, 2]

$$F_{Magnus} = \rho\kappa h \left(\mathbf{v}_s - \mathbf{v}_v\right) \times \hat{k} \tag{1.3}$$

1.7 Anomalous Freedecays

Our study begins with a survey of the experimental parameters of the anomalous free decays. Out of several thousand free decays that were preserved in the laboratory's files on paper traces, 732 were found to display some form of anomalous behavior of the two types described earlier in Section 1.4. What percentage this is of the total number of freedecays is unknown as data were commonly saved only if they showed some characteristics of interest due to the high cost of computer memory and the inconvenience of printing paper traces. In addition, at the time only the low amplitude behavior was of direct experimental interest. These anomalous freedecays were catalogued in a Microsoft Excel spreadsheet incorporating identifying information for each freedecay, resonant frequency, mode, third sound speed c_3, decay constants Q for the high and low amplitude regions, electronics calibration values, instrument time constants, critical amplitudes and velocities, and film thickness h. While temperature was not recorded on the spreadsheet, no temperature dependence was observed. In addition, graphs of various parameters showed no apparent dependence on resonator mode number m (Figure 1.5) or film thickness h (Figure 1.6.)

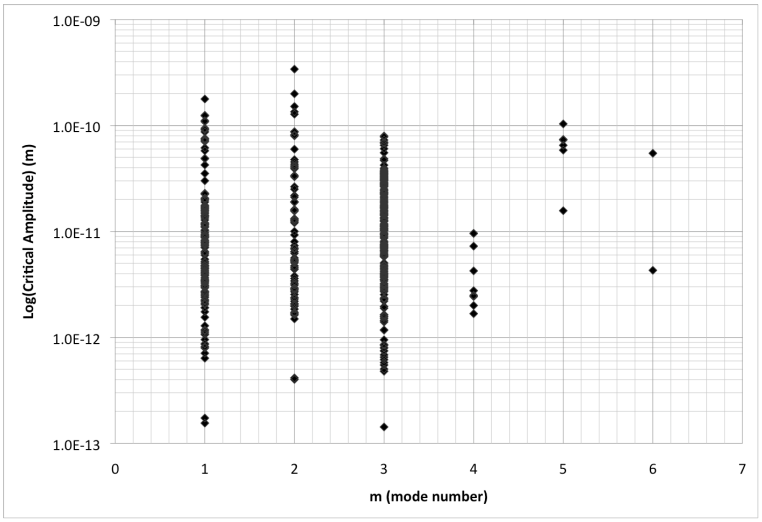

Figure 1.5: Graph of the observed dependence of the critical amplitude on mode number m.

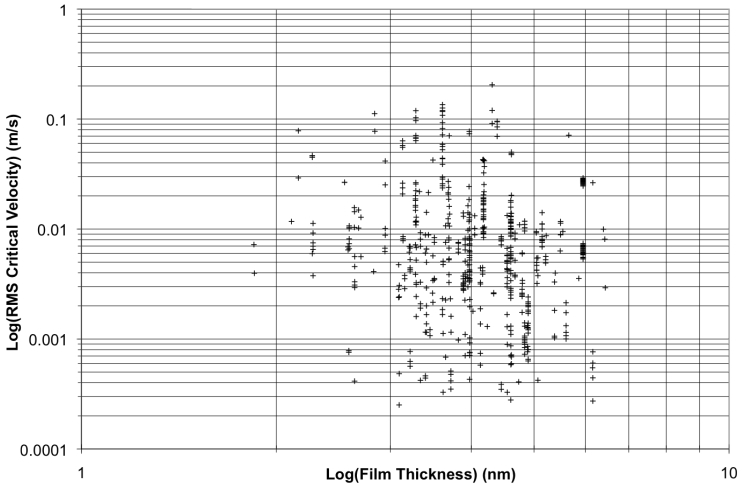

Figure 1.6: Graph of the observed dependence of the critical velocity on film thickness h.

In addition, an analysis of the mode resonant frequencies determined that all of the anomalous freedecays took place in the standing-wave modes as opposed to the rotating modes. This analysis was based on the work of Hai Luo and made use of the two-level system analysis he applied to the third sound resonators. [5]

1.8 Summation

The following work will attempt to explain and further understanding of these anomalous freedecays. This will be performed through the proposal of possible models attempting to explain the observed characteristics and the subsequent testing of their validity. Attempts will also be made to ascertain outside these models more about the nature of the mechanisms at work within these anomalous freedecays.

Chapter 2

Models

In this chapter, we will now propose and test several models:

1. A vortex friction model, based upon the pinning and depinning of vortices, which will be seen to be incomplete and unable to fully explain the observed behavior.

2. A modified vortex friction model including an additional energy associated with vortex creation, which will be seen to provide a much better explanation for the observed behavior and enable the derivation of a number of vortices involved in the dissipation. This number will be seen to be rather small (approximately three,) which is contrary to the predictions of previous work on this topic.

3. A mutual friction-based vortex dissipation model, which will be shown to be inconsistent in several aspects with the observed behavior.

4. A viscous-type drag model with an arbitrary dissipation mechanism, which

will be seen to be inconsistent with the observed behavior.

All of these models are based upon experimentally well-established quantized vortex phenomena in bulk superfluid helium and are simply extensions of these observed bulk vortex properties into the adsorbed film case. This chapter will test these various vortex dissipation models for their consistency with the observed anomalous freedecays discussed in the previous chapter.

2.1 Friction Model

In an article published in 1991 Fred Ellis and Hai Luo posited that the critical velocity phenomena observed in the free decays were the result of the pinning and unpinning of vortices from the resonator substrate. This process is analogous to a classical friction force and may be modeled as such. Ellis and Luo were motivated by the fact that free decays that display "bulge-like" non-linearities on a logarithmic amplitude vs. linear time plot appear to be linear on a linear amplitude vs. time plot. This phenomenon can be seen in Figure 2.1.

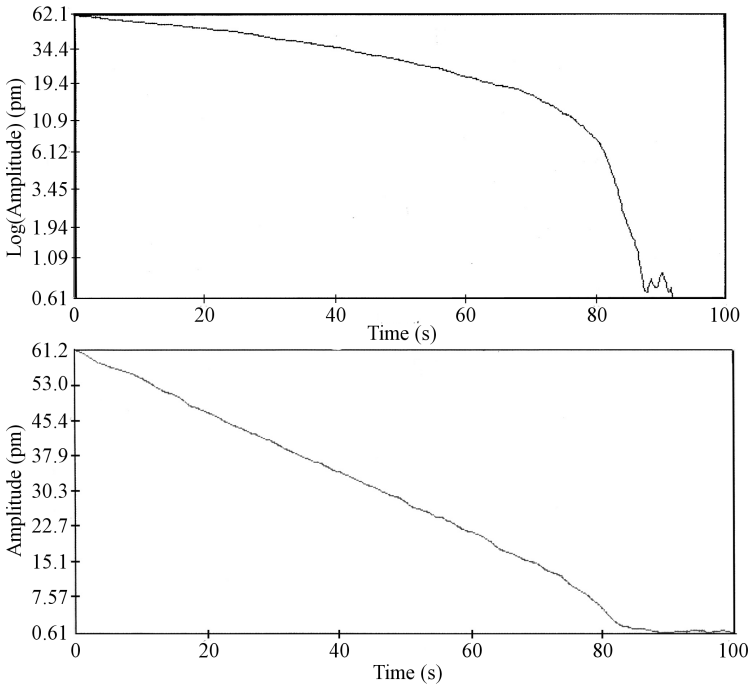

Figure 2.1: An example of an anomalous free decay, displaying a "bulge-like" non-linearity on semi-logarithmic (top) and linear (bottom) scales. Note the straight line on the linear plot.

In this first and simplest "friction model," below critical velocity flow in the film the vortices are strongly pinned to surface roughness or defects. As flow velocity increases above critical, the Magnus force is sufficient to depin the vortices from the defects. The vortices now drag upon the substrate dissipating energy (proportional to the displacement) as they encounter defects on it. This can be seen as the analog of a friction force, not unlike dragging an object along a cobblestone street. Along with the return of the oscillating flow to sub-critical velocities the vortex pins itself to a substrate defect and the pinning/depinning

process begins again. This is illustrated in Figure 2.2.

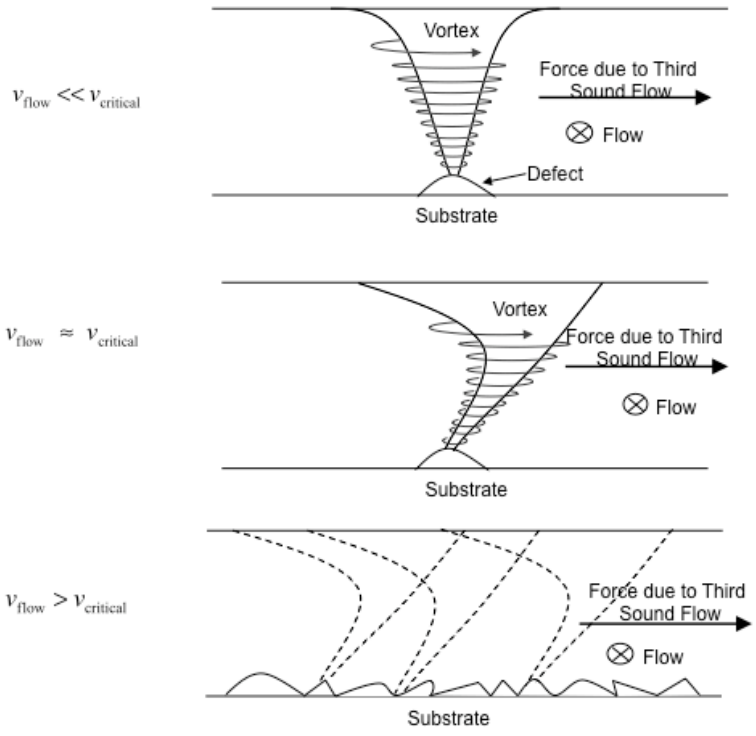

Figure 2.2: Illustration of the pinning, depinning process.

Within the article, Ellis and Luo calculated that for a particular decay this friction-like force would need to have a strength of $1.3 \times 10^{-9}\,\mathrm{N/m^2}$. [6] In keeping with this previous work, the first model considered was based upon this frictional force. The model was used to discover three important characteristics of the anomalous free decays:

1. To find how a vortex moves in a sinusoidal flow.

2. To find the energy dissipated vs. amplitude of the oscillating flow.

3. To use the model's dissipation to find the decay of the resonance.

It was assumed that the pinning force was equal to some constant $f_\circ$ determined by the averaged pinning strength of the substrate defects, resulting in a force given by:

$$\mathbf{f}_{drag} = f_\circ(-\hat{v}_v) \tag{2.1}$$

where $f_\circ$ is the strength of the friction force and $\hat{v}_v$ is the direction of vortex motion. First, we sum this force with the Magnus force in the usual Newtonian way employing the no-net-force assumption that is regularly used with superfluid vortices. While the vortices may be treated as objects due to the extent of their cores, these cores are presumed to be absent of fluid and to have very thin walls. The superfluid vortices are thus presumed to be massless and hence due to Newton's Second Law, the net force upon them, $\mathbf{F}_{vortex}$, must be 0. With this assumption, the summation becomes:

$$\mathbf{F}_{vortex} = \rho\kappa h\left(\mathbf{v}_s - \mathbf{v}_v\right) \times \hat{k} - f_\circ \hat{v}_v = 0 \tag{2.2}$$

This allows us to find the components of the velocity perpendicular and parallel to the direction of flow:

$$\begin{bmatrix} v_{v\parallel} \\ v_{v\perp} \end{bmatrix} = \begin{cases} \begin{bmatrix} 1 - \left(\frac{v_c}{|\mathbf{v}_s|}\right)^2 \\ \left(\frac{v_c}{|\mathbf{v}_s|}\right)\sqrt{1 - \left(\frac{v_c}{|\mathbf{v}_s|}\right)^2} \end{bmatrix} |\mathbf{v}_s| & \text{if} \quad |\mathbf{v}_s| > v_c \\ \begin{bmatrix} 0 \\ 0 \end{bmatrix} & \text{if} \quad |\mathbf{v}_s| < v_c \end{cases} \tag{2.3}$$

where v_c is the magnitude of the critical velocity and $\mathbf{v}_s$ is the flow velocity.

We can then integrate to find the average power dissipated by a single vortex

using the following equation:

$$P_{AV} = \frac{1}{T}\int_0^T \mathbf{f}_{drag} \cdot \mathbf{v}_v dt \tag{2.4}$$

where T is the period of oscillation.

We introduce the scaling $A = \eta/\eta_c = |\mathbf{v}|/v_c$. This greatly simplifies matters as now all amplitudes η will be scaled to the critical amplitude η_c, a quantity that can be read directly from the experimental data. Using this scaling, the equation takes the form of the curve seen in Figure 2.3.

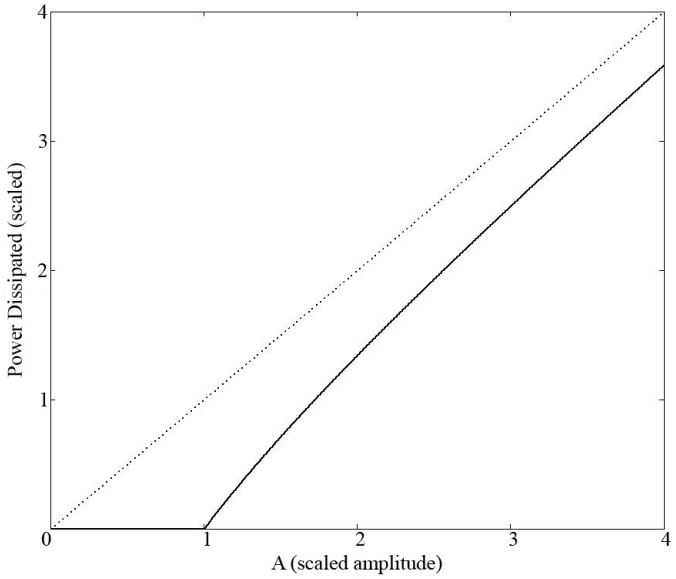

Figure 2.3: Scaled power dissipated as a function of amplitude A scaled to the critical amplitude.

This average power P_{AV} can be multiplied by a number of vortices per area n

and decomposed in the following manner:

$$W(A) = P_{AV} n \tag{2.5}$$

This $W(A)$ can then be combined with a background exponential dissipation to produce the total energy lost in the wave:

$$\frac{dE(A)}{dt} = -W(A) - \frac{\omega_\circ E(A)}{Q_\circ} \tag{2.6}$$

E(A) is the energy in the wave, which is twice the kinetic energy, given by:

$$E(A) = \frac{1}{2}\rho h v_c^2 A^2 \tag{2.7}$$

Substituting this energy into Equation 2.6 and solving for dA/dt results in:

$$\frac{dA}{dt} = \frac{f_\circ v_c n}{\pi}\left(\frac{1}{2}\rho v_c^2\right)^{-1}\frac{I(A)}{A} - \frac{\omega_\circ}{2Q_\circ}A \tag{2.8}$$

where $I(A) = \int_{\sin^{-1}\left(\frac{1}{A}\right)}^{\frac{\pi}{2}} \sqrt{A^2 \sin^2\phi - 1}\, d\phi$, a factor that is simply a scaled version of Equation 2.4.

We now introduce some scaling to simplify this equation, letting:

$$\alpha = \frac{2 f_\circ n}{\pi \rho h v_c} \tag{2.9}$$

$$\tau = \alpha t \tag{2.10}$$

$$\gamma = \frac{\omega_\circ}{2Q_\circ}\frac{1}{\alpha} \tag{2.11}$$

It becomes clear now through dimensional analysis that α is some type of rate constant and γ is a scaled decay constant. By employing this scaling Equation 2.8 reduces to:

$$\frac{dA}{d\tau} = -\frac{I(A)}{A} - \gamma A \tag{2.12}$$

This is a separable differential equation, so separating and integrating results in:

$$\tau = -\int_1^A \frac{A}{I(A) + \gamma A^2}\, dA \tag{2.13}$$

Note from the above choice of limits that $\tau = 0$ at $A = 1$, the critical amplitude. This allows us to easily identify the critical point both in scaled amplitude and time. Inverting this equation produces the amplitude Y as a function of τ:

$$Y(\tau) = Y_c \,\mathrm{Amp}(\gamma, \tau) \tag{2.14}$$

Amp is a numerically defined function involving the two non-analytic integrations of Equation 2.13 and the inversion from $\tau(Y)$ to $Y(\tau)$. The critical amplitude Y_c is now in Y scale units (normally nanometers.) In order to produce a usable fitting function, we make the final substitution $\tau = \alpha(t - t_\circ)$ where $t_\circ$ is now the origin of laboratory time. This results in the final fitting function:

$$Y(t) = Y_c \,\mathrm{Amp}(\gamma, \alpha(t - t_\circ)) \tag{2.15}$$

This function most certainly has the ability to produce graphs that qualitatively resemble those of the target data. This qualitative resemblance is clearly illustrated in Figure 2.4.

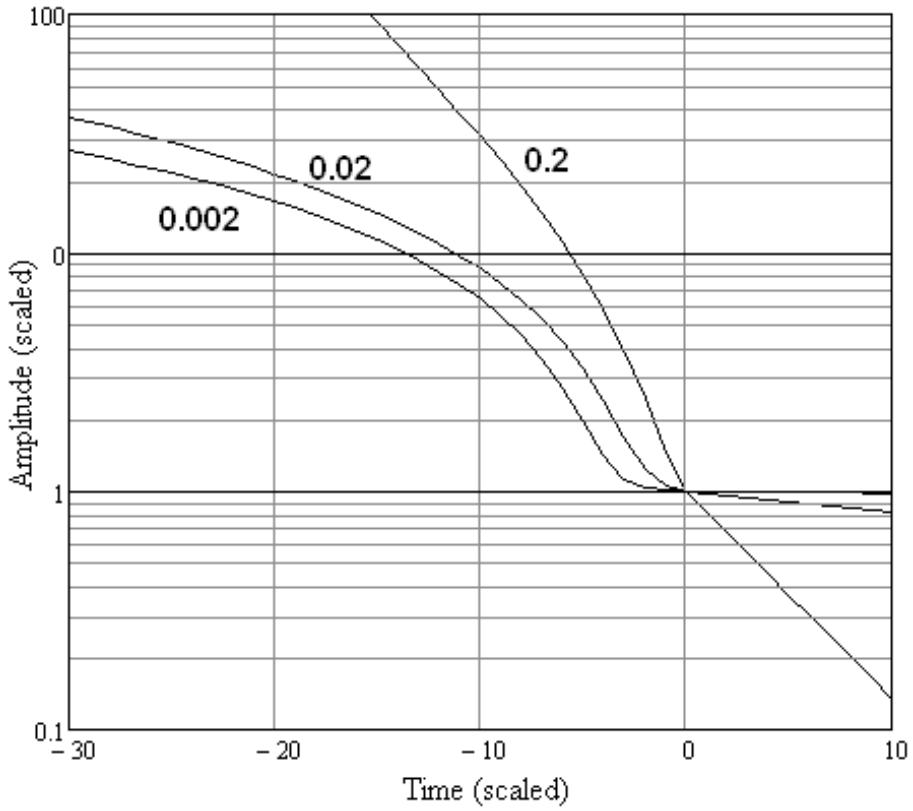

Figure 2.4: Output of the Y function on a logarithmic scale, with time scaled to the critical time. The graphs correspond to varying values of γ.

This function was fit to the experimental data using the three parameters Y_c, α, and $t_\circ$. The scaled background decay constant γ was fit by hand separately to the portion of data below the $A = 1$, $\tau = 0$ critical point. This was an effort to maintain the computation time within reasonable bounds.

The laboratory data was extracted from the original dot-matrix printed paper traces via a pixel averaging methodology. The paper graphs of interest were first scanned at 300dpi. The images were then aligned and cropped to the middle

pixels of the axes using photo-manipulation software. The remaining axis pixels and any imperfections such as smudges or paper-yellowing were then removed. The resulting image was then converted to a monochrome image using a 50% brightness threshold. That is, all pixels above 50% in brightness were converted to black and all below that threshold were converted to white. Subsequently each column (or binned group of columns) of pixels was averaged to produce a single data-point centered within the trace line which was then scaled based on its vertical position in the image to produce an actual datapoint value for that point. This procedure was necessary as commercially available data-extraction software was unable to produce accurate traces due to the multiple pixel width of the trace line and the sometimes significant noise present in the traces. Inherent in this procedure is that averaging over noise is a completely automated process, removing the human intervention required by the commercial software.

A nonlinear, least-squares Levenberg-Marquardt fitting routine was used to fit the laboratory data to this function. Unfortunately, there was a lack of sufficient parameters to properly fit the curves in question. This can be seen clearly in Figure 2.5, the graphs of two separate data sets fit using this model. These results are typical of the fit curves produced by this model. The top graph of the figure exhibits one common issue with these fits, as the low amplitude behavior corresponds quite well to the data sets, but the high amplitude regime lacks sufficient curvature to match the actual data. The lower graph of the figure is able to match the high amplitude behavior reasonably well, but the low-amplitude regime fails to match the actual data.

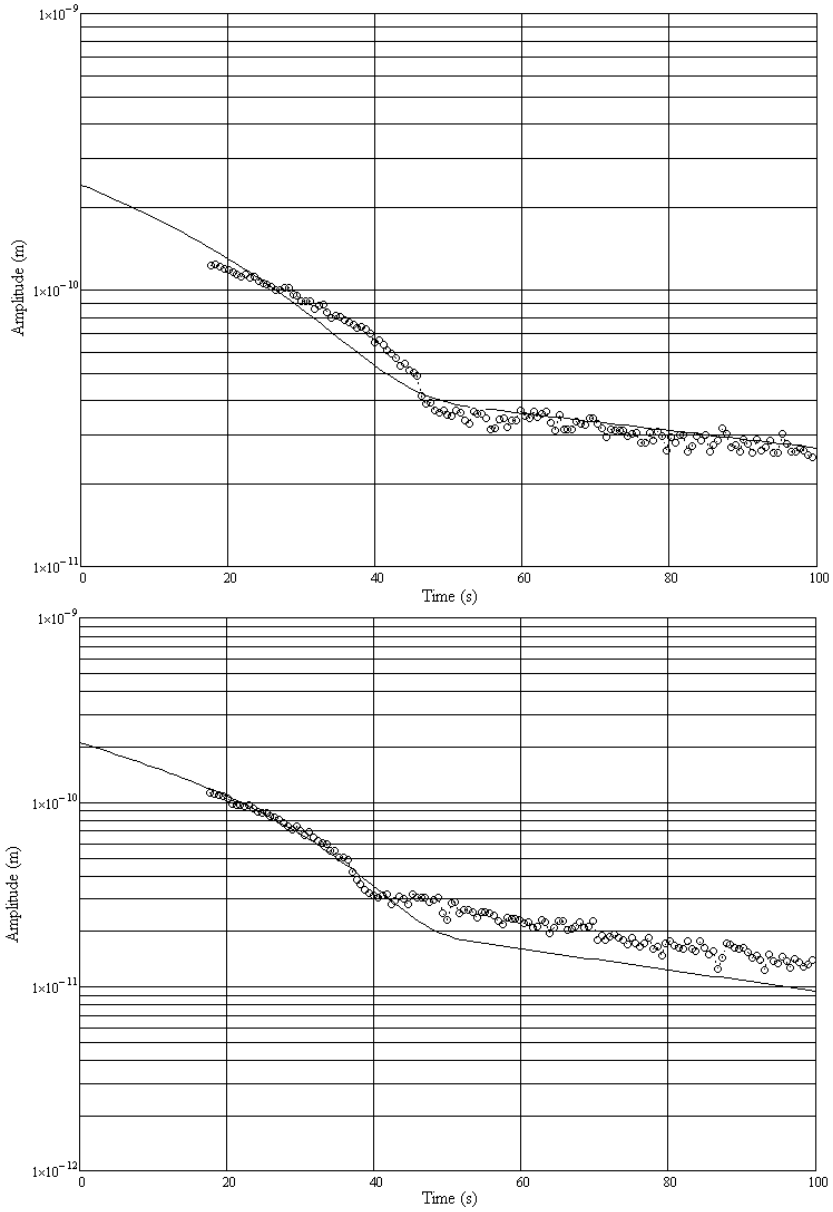

Figure 2.5: Illustrations of the best fits using the friction model of two separate data sets. The dotted data sets are the actual data to which the solid lines are fitted. Note the lack of correspondence between the fit curves and the data.

Attempts were made to determine whether there was a technical explanation for these issues including fitting the logarithm of the data, adjusting the convergence tolerance of the fitting algorithm, and extensive attempts to improve the fit by manually manipulating the parameters. The conclusion was reached that no improvement of the fit curves was obtained through any of these exercises and that the model itself must be fundamentally incomplete as it lacks sufficient physics to properly fit this data. As one can see in Figure 2.5, as discussed above there is no way to simultaneously achieve both the necessary curvature for the high-amplitude regions and a sufficiently sharp transition at the critical point. The friction model can produce either curvature or kink, but not both, so some fundamental piece of the physics must be missing.

2.2 Dissipation Function

It was realized that it would be possible to derive numerically a dissipation function from the experimental data without reliance on a particular model, such as the friction model discussed above. We begin with a generalized free decay relationship with a background dissipation based on a quality factor $Q_\circ$ and an added dissipation term $W(A)$:

$$\frac{dE}{dt} = -W(A) - \frac{\omega_\circ E}{Q_\circ} \tag{2.16}$$

where E is the total energy of the third-sound wave and $\omega_\circ$ is the wave frequency. Letting $E = \alpha\eta^2$ and making appropriate substitutions allows us to reach the following form:

$$\frac{d\eta}{dt} = -\frac{W}{2\alpha\eta} - \frac{\omega_\circ \eta}{2Q_\circ} \tag{2.17}$$

Dividing through by the critical amplitude η_c and solving for the added dissipation $W(A)$ results in:

$$W(A) = 2\alpha A\eta_c^2 \left(\frac{dA}{dt} + \frac{\omega_\circ A}{2Q_\circ} \right) \tag{2.18}$$

The only wrinkle remaining is to solve for α, which is dependent on resonator geometry, oscillation mode, and film conditions. The total energy of the third sound wave is two times the kinetic energy, given by:

$$E = s\frac{1}{2}\rho h a \bar{v^2} \tag{2.19}$$

Here ρ is the density of ^{4}He, h is the mean thickness of the film, a is the area of the cell, and $\bar{v^2}$ is the mean-square velocity averaged over the cell. We first convert our amplitude data η into a velocity v by multiplying by the third sound propagation speed c_3 and dividing by the film thickness h. We perform the averaging by multiplying by the root-mean-square average of the standing-type wave function, J_{RMS} for the particular mode, giving a mean-square velocity average like so:

$$\bar{v^2} = c_3^2 \frac{\bar{\eta^2}}{h^2} = \left(c_3 \frac{\eta}{h} \right)^2 J_{RMS}^2 \tag{2.20}$$

Finally, s is a parameter that denotes whether the wave is of the standing ($s = 1$) or traveling ($s = 2$) type. Setting Equation 2.19 equal to $\alpha\eta^2$ and solving for α gives for the traveling wave case:

$$\alpha = J_{RMS}^2 \frac{\rho a c_3^2}{h} \tag{2.21}$$

where c_3 is the third sound speed and J_{RMS} is the average of the standing wave function, given by:

$$J_{RMS}^2 = \frac{1}{\pi x_{mn}^2} \int_0^{x_{mn}} \int_1^{2\pi} J_m(x) x \; dx d\phi \tag{2.22}$$

$$= \frac{1}{2}\left[1 - \left(\frac{m}{x_{mn}}\right)^2\right] J_m(x_{mn})^2 \tag{2.23}$$

Here x_{mn} is the n^{th} zero of the derivative of the Bessel function of the first kind J_m. The integer numbers m and n designate and describe the particular third sound mode of interest, as m is the azimuthal wave number and n is the radial wave number.

Now, all parameters in the dissipation equation (Equation 2.18) are known. The scaled amplitude A can be extracted from the data by fitting the data to an appropriate function and then substituting that fit function and its derivatives into the dissipation equation. This fitting of the data is necessary because using the data directly in Equation 2.18 would result in unmanageable amounts of noise. This is due to the necessity of taking a derivative dA/dt of the already noisy data. The function to which the data was fit, overcoming this issue, was:

$$d(a, \beta, x_\circ, t_\circ, t) = \exp\left[\frac{-(t - t_\circ)\omega_\circ}{2Q_\circ}\right] + \begin{cases} a(t_\circ - t) + \beta - \frac{\beta}{1 + \frac{t_\circ - t}{x_\circ}} & \text{if } t > t_\circ \\ 0 & \text{otherwise} \end{cases} \tag{2.24}$$

This function incorporates the known background damping in the first term. The piecewise-defined second term was employed because the first two terms $a(t_\circ - t) + \beta$ of the $t > t_\circ$ part is linear, corresponding to the approximately linear behavior

of the high-amplitude region. At these high amplitudes, the third term $-\frac{\beta}{1+\frac{t_\circ - t}{x_\circ}}$ is rather small owing to a large denominator. As the amplitude approaches the kink point at $t = t_\circ$ the denominator of the third term decreases drastically, increasing its influence upon the linear and providing the appropriate curvature. After the critical point at $t = t_\circ$ there is only background damping present, as reflected in the second case of the piecewise function. This function provides rather good fits to the experimental data as can be seen in Figure 2.6.

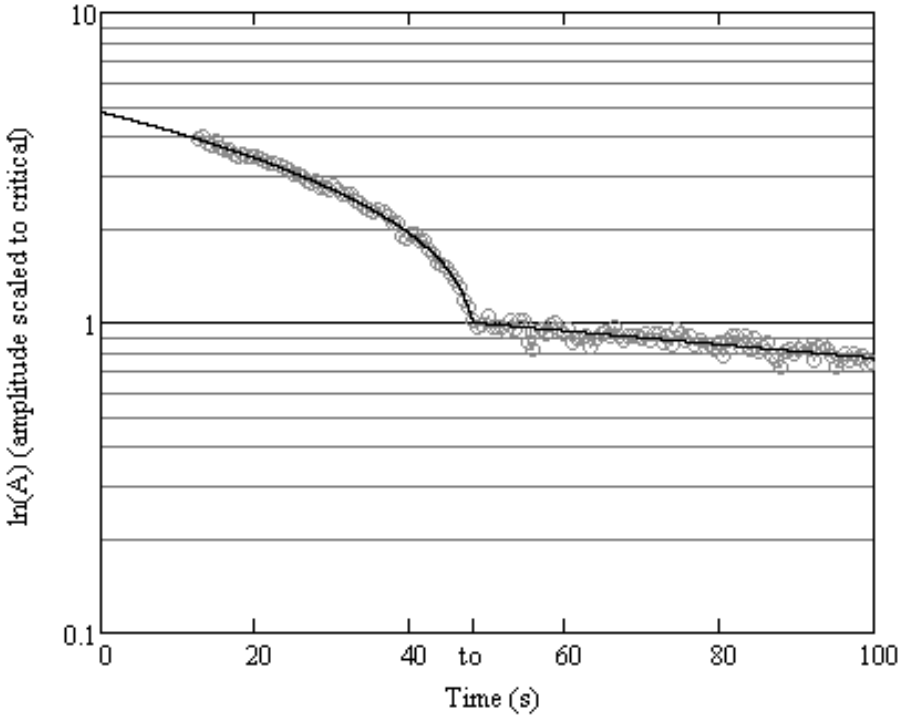

Figure 2.6: Illustration of the fit between Equation 2.24 and actual data displaying the curved transition between slopes. The dotted data sets are the actual data to which the solid lines are fitted.

An example of the resulting power dissipation functions is shown in Figure

2.7. Note the discontinuity that is characteristic of this function. At $A = 1$, the critical amplitude, the power jumps up to nearly 4×10^{-15} Watts and then decreases rapidly before slowly rising again, only reaching the same level as at $A = 1$ just before $A = 5$, nearly five times the critical amplitude.

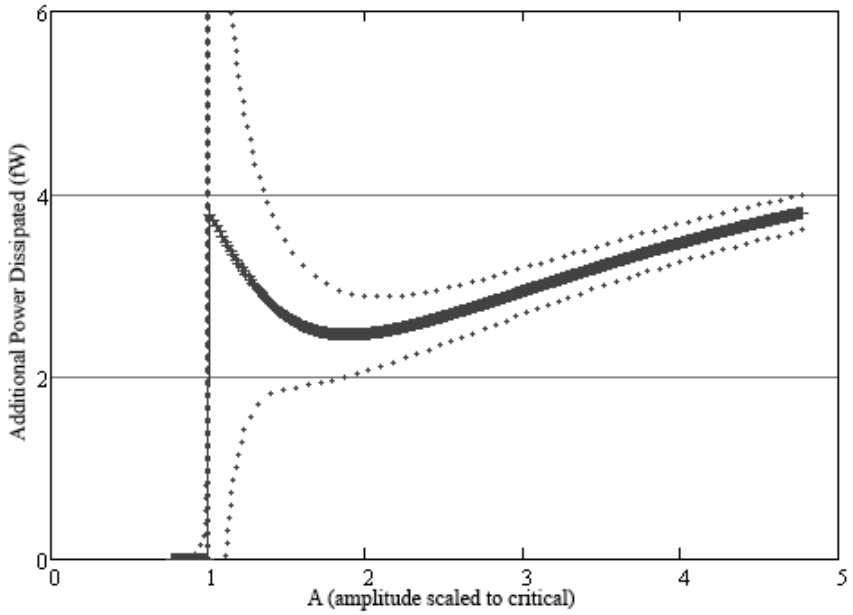

Figure 2.7: Graph of a power dissipation function derived directly from experimental data. The dotted curves bracketing the data are the upper and lower bounds of error.

When compared with the known dissipation of a given model, a number of vortices can be extracted by simply dividing the experimentally derived dissipation function by the theoretical dissipation of a model for a single vortex. This was performed using the friction model's dissipation for one vortex (derived earlier in

Equation 2.8,) given by:

$$W_{friction}(A) = \begin{cases} \frac{4\pi\hbar c_3^2 \eta_c^2}{m_4 h} \int_{\arcsin \frac{1}{A}}^{\frac{\pi}{2}} \sqrt{A^2 \sin x^2 - 1}\, dx & \text{if } A > 1 \\ 0 & \text{otherwise} \end{cases} \tag{2.25}$$

The N number of vortices in the cell produced by dividing the experimental data by this equation is shown in Figure 2.8. Note that the number of vortices is notably non-constant, increasing multiple orders of magnitude in the region between $A = 2$ and $A = 1$. At higher amplitudes the number of vortices appears to level off at approximately 16. If anything, one would expect more vortices at higher amplitudes, not fewer. One way to remedy this non-physical result is to introduce some form of additional energy dissipation that is not accounted for in the friction model, as is done in the following section.

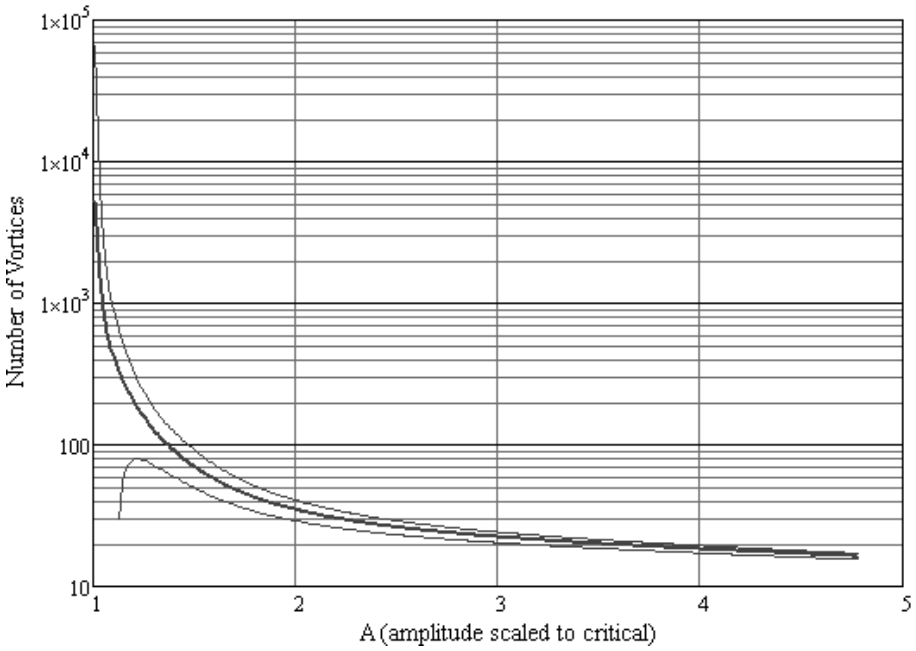

Figure 2.8: Graph of the number of vortices in the cell derived from experimental data and the friction model.

2.3 Creation Energy

This additional energy term was introduced in an effort to attain a relatively constant number of vortices throughout the wave cycle. This additional dissipation above and beyond that predicted by the friction model holds promise to tame the many orders of magnitude spikes in the number of vortices predicted by the friction model alone as shown in Figure 2.8. It is also known that these vortices have an energy (with both kinetic and potential terms) associated with them. While this addition to the model is simply speculative as far as the mechanisms at work are concerned, we will see that this additional bit of physics appears to

fit the observed data quite well. Numerically, this added term was included in the full-wave energy function from before:

$$\frac{dE}{dt} = -W(A) - \frac{\omega_\circ}{Q_\circ}E - u_\circ\frac{dN}{dt} \tag{2.26}$$

where the first two terms are as in Equation 2.16. The new term is the $u_\circ\frac{dN}{dt}$ where $u_\circ$ is an energy parameter and $\frac{dN}{dt}$ is the rate of change of vortex creation. The entire term can be expressed as W_c, the "creation energy."

Manipulating the equation as in the previous section allows us to produce a dissipation function and number of vortices. This results in an equation for the dissipation given by:

$$W_\circ = -2\alpha A\eta_c^2\left(\frac{dA}{dt} + \frac{\omega_\circ}{2Q_\circ}A\right) - W_c \tag{2.27}$$

The number of vortices that results is given by:

$$N(A) = \frac{W_\circ(A)}{W_1(A) + \frac{\omega_\circ}{\pi}u_\circ} \tag{2.28}$$

where W_1 is the dissipation of the model of interest, in this case the friction model.

A simple hand fit of the data was used at first to derive a value for $u_\circ$. The only criterion for these values was to reduce the number of vortices with amplitude as much as possible. As flat a curve as possible was the goal. The results of this effort can be seen in Figure 2.9. As one can see in this figure, the bottommost of the graphs, corresponding to $u_\circ = 8 \times 10^{-19}$ J, displays the smallest deviation from a constant number of vortices.

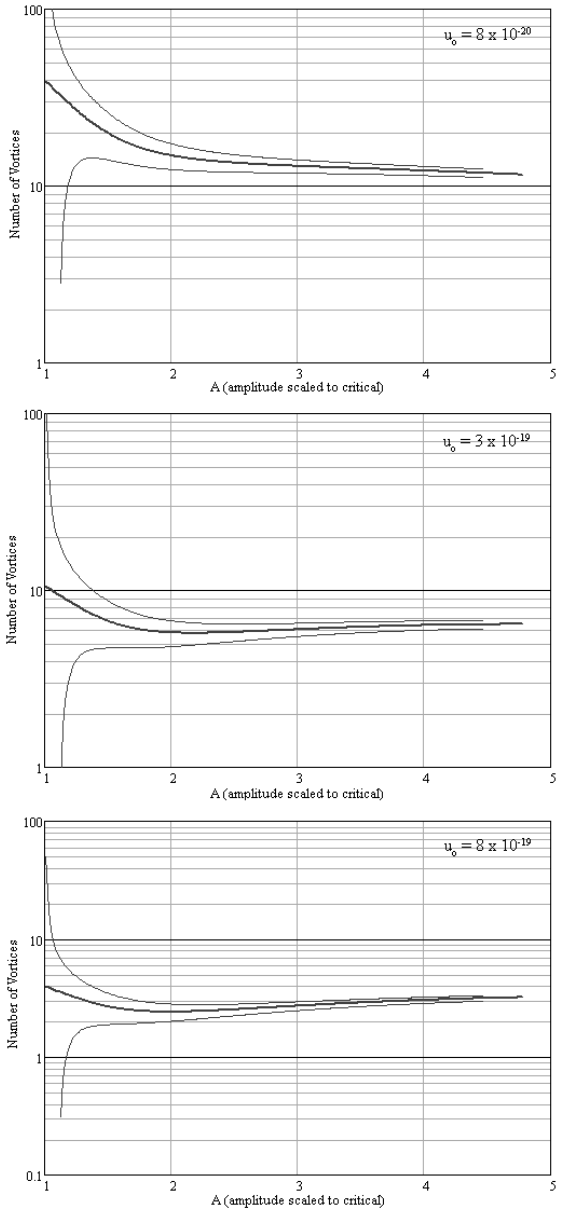

Figure 2.9: Number of vortices vs. scaled amplitude on a semi-logarithmic plot for varying values of $u_\circ$. The upper and lower functions are the upper and lower bounds of the error.

It is this flattest fit that implies that for the friction model, there must be approximately three vortices each with a dissipation of 8×10^{-19} J beyond that already accounted for in the friction model. This number of three can be seen from the high amplitude limit of the graphs, at which there should be no variation in the number of vortices involved. The value of three is an average based on applying this procedure to multiple data sets displaying the bulge-like anomaly. This is a crucial outcome of the investigation as it implies that these anomalous dissipations are the result of a very small number of vortices. Before this point, the number of vortices involved in these additional dissipative processes was not known. This energy value $u_\circ = 8 \times 10^{-19}$ J corresponds to the energy in an area of the total wave of $2.885 \times 10^{-9}\,\mathrm{m}^2$ or approximately a $60\,\mu$m diameter circle at the critical velocity.

To give a point of comparison for this value for $u_\circ$ we must turn to the physics of a likely cause for this creation energy term. It was postulated that this additional dissipation might be associated with the creation of vortices within pockets of bulk helium liquid trapped by defects in the experimental cell, either within the substrate or the epoxy joint joining the outer glass plates of the cavity cell resonator. The exact microscopic processes behind vortex nucleation in superfluid helium are not well understood, but one theory is that the process of vortex ring formation is started by thermal excitations, in this case in the pocket of bulk fluid, and then progresses in size due to the film flow until a certain critical energy is reached and the vortex ring breaks into a vortex/anti-vortex pair (an inherently lower energy state.) [1, 2, 7] Figure 2.10 provides an illustration of this process.

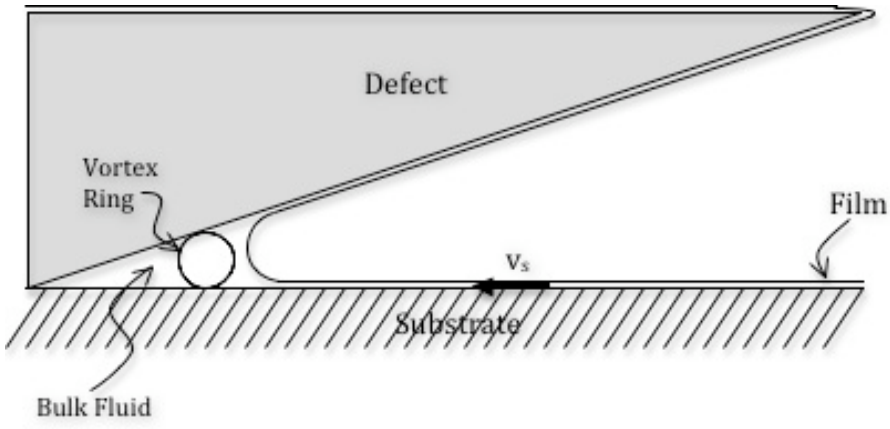

Figure 2.10: Illustration of the vortex nucleation process inside a pocket of bulk fluid.

Deriving a creation energy from this model requires the energy of a pocket of bulk fluid in the film. This kinetic energy is the vortex creation energy. For a pocket of non-film fluid of size L, the kinetic energy is given by: [2]

$$E(L) = \frac{\frac{1}{2}\left(2\pi\frac{\hbar}{m_4}\right)^2 L \ln\left(\frac{L}{a_\circ}\right)}{k} \tag{2.29}$$

Here, m_4 is the mass of a ^{4}He atom, 6.646×10^{-27} kg, $a_\circ$ is the width of a superfluid vortex core, 1.3 Å and k is the Boltzmann constant. L is related to the thickness of the film h via the relationship:

$$h = \left(\frac{kT_vL}{\gamma}\right)^{\frac{1}{3}} \tag{2.30}$$

where T_v is the van der Waals force constant in Kelvin and γ is the surface tension,

This allows us to find the creation energy quite simply and directly from the

film thickness h, a known experimental quantity. The creation energy $u_\circ$ derived for the same experimental data set as in Figure 2.8 is 8.201×10^{-21} J. This results in the graph shown in Figure 2.11.

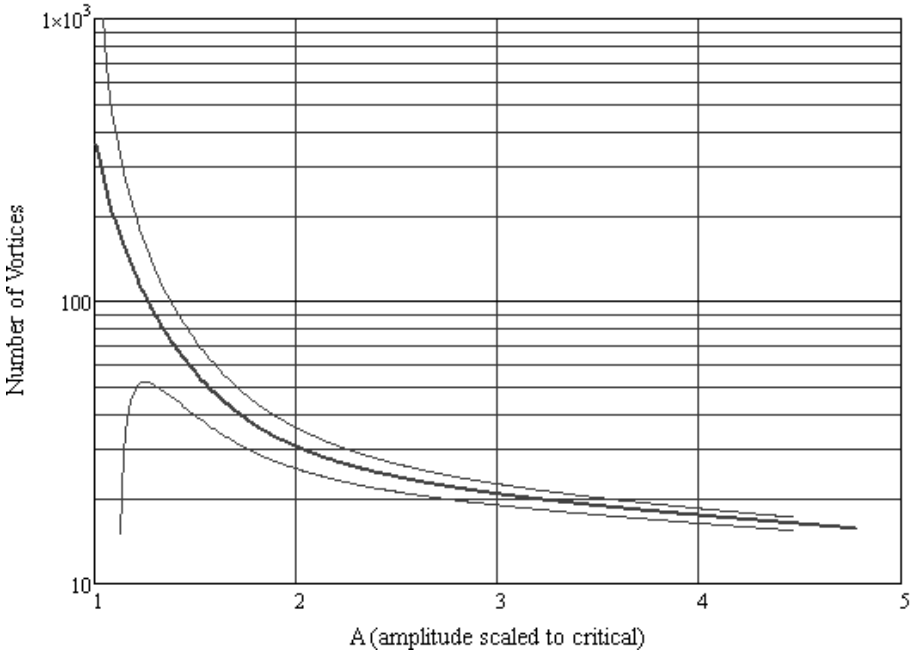

Figure 2.11: Number of vortices vs. scaled amplitude on a semi-logarithmic plot for $u_\circ = 8.201 \times 10^{-21}$ J as determined by the vortex ring nucleation calculations. The upper and lower functions are the upper and lower bounds of the error.

As we can see, the two values for $u_\circ$ are not in agreement. In fact, they differ by two orders of magnitude. As stated earlier, the processes of vortex nucleation in superfluid are not well understood and this may account for the discrepancy. The mechanism responsible for the creation of vortex rings in these pockets may not fully account for the total energy required to create vortex pairs. Hence, we conclude that pocket vortex creation is not sufficient.

2.4 Viscous Model

We turn now to the other type of anomalous free decays, the "kink" type. In this variety of anomalous free decays, the data displays one characteristic decay constant Q_1 at high amplitudes and then transfers to a decay with another decay constant $Q_\circ$ at some critical amplitude, without displaying much in the way of transition behavior. It is this absence of a transition that differentiates these free decays from those analyzed thus far in this chapter. Referring between Figure 2.1 and Figure 2.12 quickly makes this distinction clear.

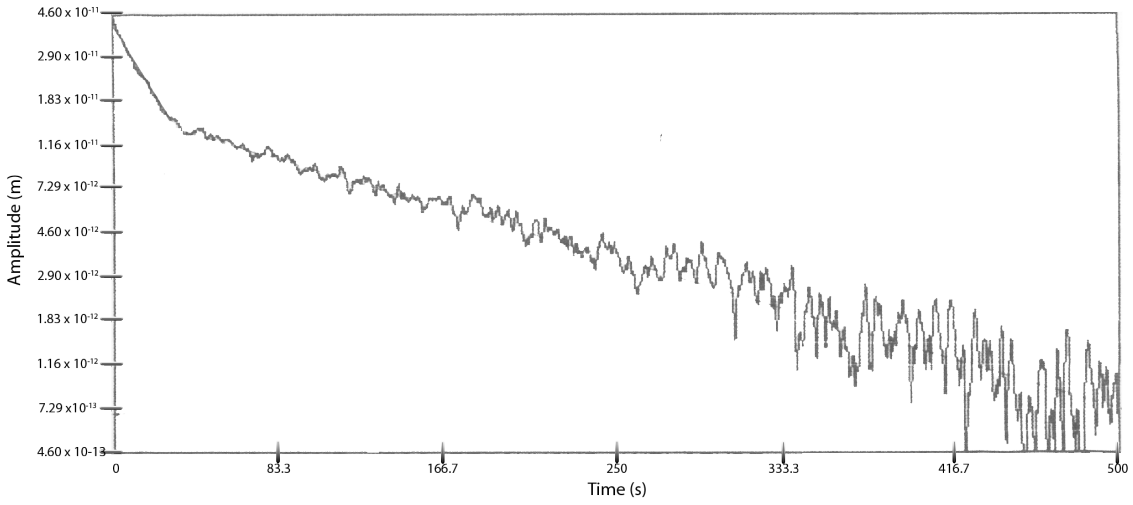

Figure 2.12: An example of an anomalous free decay, displaying a "kink-like" nonlinearity on a semi-logarithmic scale.

These types of decays require another model for the dissipative effects. This need can be seen by referring to Figure 2.4. There is no value of the parameter γ that would provide both sufficiently linear transition behavior and an appropriate slope corresponding to $Q_\circ$ at sub-critical amplitudes.

The new model is based upon a viscous drag force that is a result of mutual friction between the vortex and and the gas of thermal excitations that is the normal fluid component of the two-fluid model. [1] Like most drag forces, this one is also proportional to the velocity of the vortex with an unknown proportionality constant γ:

$$f_{drag} = -\gamma\left(\mathbf{v}_v\right) \tag{2.31}$$

As before, this force may be summed with the Magnus Force in the Newtonian way (with the no-net-force assumption):

$$\mathbf{F}_{vortex} = \rho\kappa h\left(\mathbf{v}_s - \mathbf{v}_v\right) \times \hat{k} - \gamma\left(\mathbf{v}_v\right) = 0 \tag{2.32}$$

The only missing piece of information for this model is a value for the coefficient γ. The entire model is based upon the phenomenon of "mutual friction," this viscous drag that results from the interaction between the normal fluid component of the fluid and the vortex. This is a well documented property, first proven by Hall and Vinen in 1956. They derived experimentally the coefficient for this force to be: [1]

$$\gamma = B\frac{\rho_s\rho_n}{2\rho} \tag{2.33}$$

where B is a constant of proportionality, equal to 4/3 in the regime this data was taken, ρ_n is the density of the normal fluid component, and ρ_s is the density of the superfluid component. As was found by Andronikashvili in 1946, below 1 K the superfluid component is nearly all of the fluid density, so it is an excellent approximation to say that $\rho_s/\rho = 1$. [1] The density of the normal fluid component

of the fluid is given by: [1]

$$\rho_n = \rho_\circ \left(\frac{T}{1\,\mathrm{K}} \right)^{1.8} \tag{2.34}$$

where $\rho_\circ = 0.0041$ and $\rho = 0.6\,\frac{\mathrm{kg}}{\mathrm{m}^3}$. This immediately begins to cast doubt upon the validity of this model as ρ_n has temperature dependence and my analysis and previous work have never seen any temperature dependence in the anomalous free decays or decay constants Q.

The same process of analysis as was employed for the friction model was applied to this model. The data was fit to Equation 2.24, as this functional form had sufficient adjustability to accommodate these types of anomalous free-decays as well. Figure 2.13 shows a typical fit, which is qualitatively quite good.

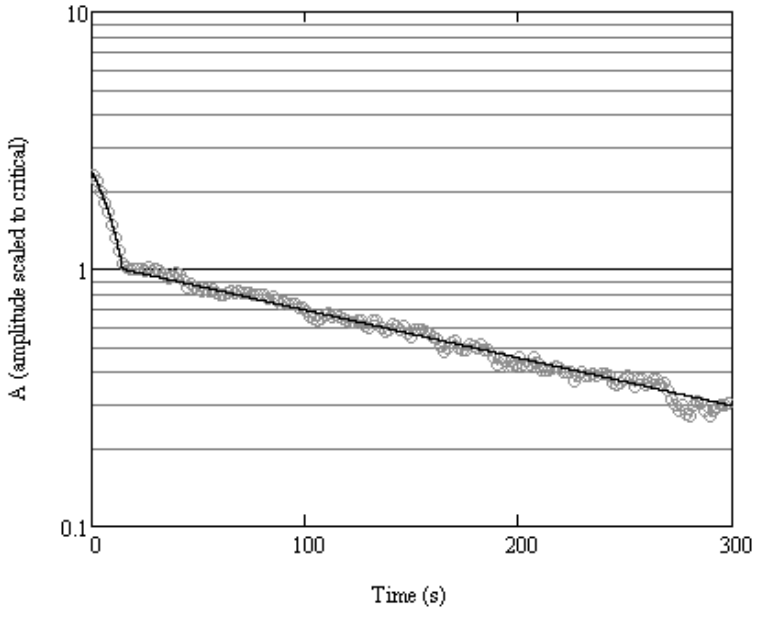

Figure 2.13: Illustration of the fit between Equation 2.24 and actual data displaying the abrupt kink-like transition between decay constants. The dotted data sets are the actual data to which the solid lines are fitted.

We then calculate a numerical dissipation function for this data, finding a total dissipation for the cell as shown in Figure 2.14.

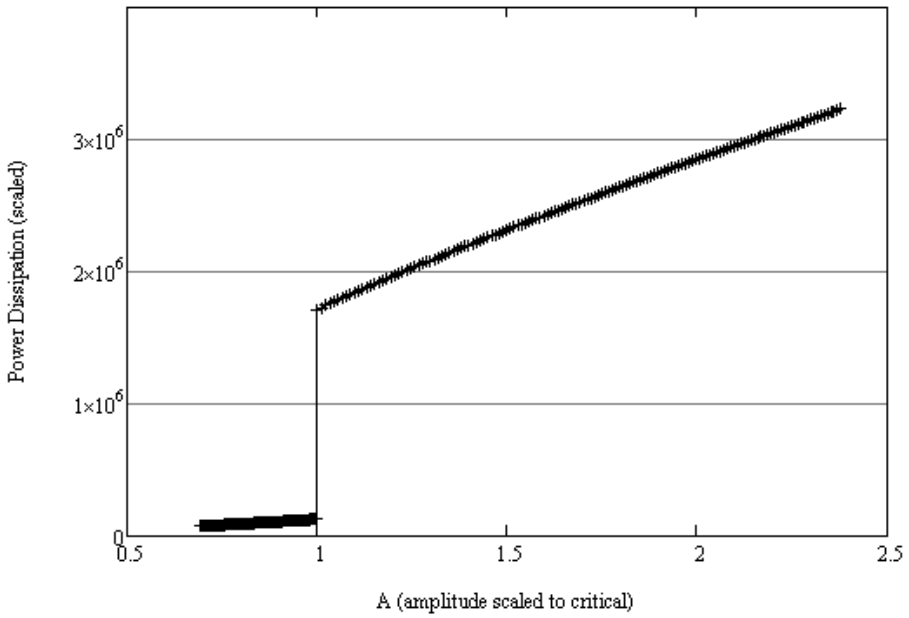

Figure 2.14: Total power dissipation in the cell modeled upon viscous drag as a function of the scaled amplitude A.

In the same way as before, an analog to Equation 2.25 was developed to describe the dissipation of a single vortex in this flow. A number of vortices was derived via the the same methodology. Dividing the total power dissipation in the cell by the amount of power dissipated by a single vortex results in a number of vortices, which is shown in Figure 2.15. As we can see, yet again, the number of vortices is not constant. While it does not range to the same degree as it did in the friction model calculation, there is still some non-constancy of the number.

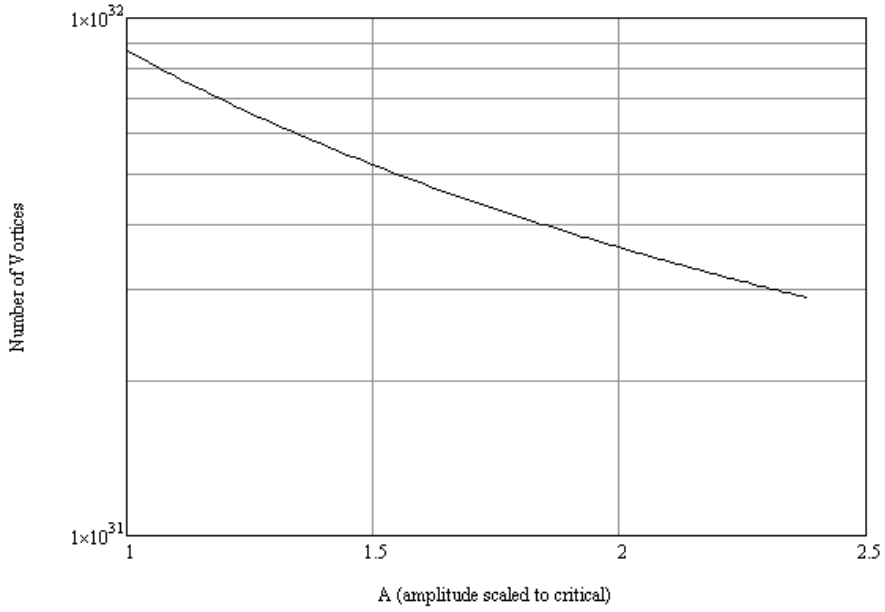

Figure 2.15: Graph of the number of vortices in the cell derived from experimental data and the viscous model on a semi-logarithmic scale.

What is highly important to take notice of is the fact that this is an extremely large number of vortices, on the order of 10^{31}. In fact, if all of these vortices had typical vortex core sizes in superfluid helium film, $a_\circ = 1.3\,\text{Å}$, the area of the cores alone, without any extent beyond them, would be 25 orders of magnitude larger than the area of the experimental cell itself. It is obvious that this model is unrealistic for the situations we are attempting to model. In addition, we see that the viscous model predicts more drag at higher velocities, which does not conform to the observed behavior of the data.

For the same motivations as before, a creation energy term was introduced in an attempt to improve the constancy of the number of vortices. A creation energy

of $u_\circ = 8 \times 10^{-19}$ J was employed. This value was chosen to maintain continuity with the previous model, under the logical assumption that the amount of energy required to create a vortex would be similar. The results of this calculation are shown in Figure 2.16. One can see that this function marginally exhibits a smaller variance of number of vortices than that without a creation energy (Figure 2.15.) What is unchanged, however is the exceptionally large number of vortices, yet again placing this model as impossible.

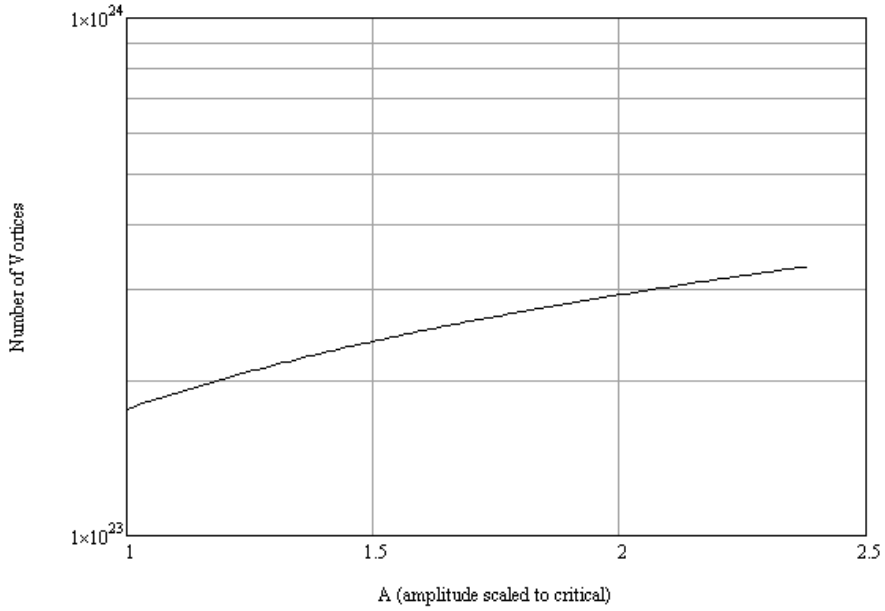

Figure 2.16: Graph of the number of vortices in the cell compensated with a creation energy term of $u_\circ = 8 \times 10^{-19}$ J derived from experimental data and the viscous model on a semi-logarithmic scale.

It has quickly become clear that the viscous "mutual friction" based model cannot be an explanation for the phenomena observed due to the lack of observed

temperature dependence and an implausible number of vortices required to be participating in the dissipative motion.

We will now propose one final modification to this viscous damping model. Instead of having the proportionality coefficient γ in Equation 2.31 determined by the known "mutual friction" force, we will instead make this coefficient a freely adjustable parameter. We will not consider what the physical cause of this force might be, but instead simply say that it is an as yet undiscovered force. The mechanics of the model would be unchanged from the "mutual friction" model, so we may simply hand-fit a value for γ. Doing this, we find that the flattest curve for the number of vortices is given by the value $\gamma = 1 \times 10^{-20}$. This curve is shown in Figure 2.17.

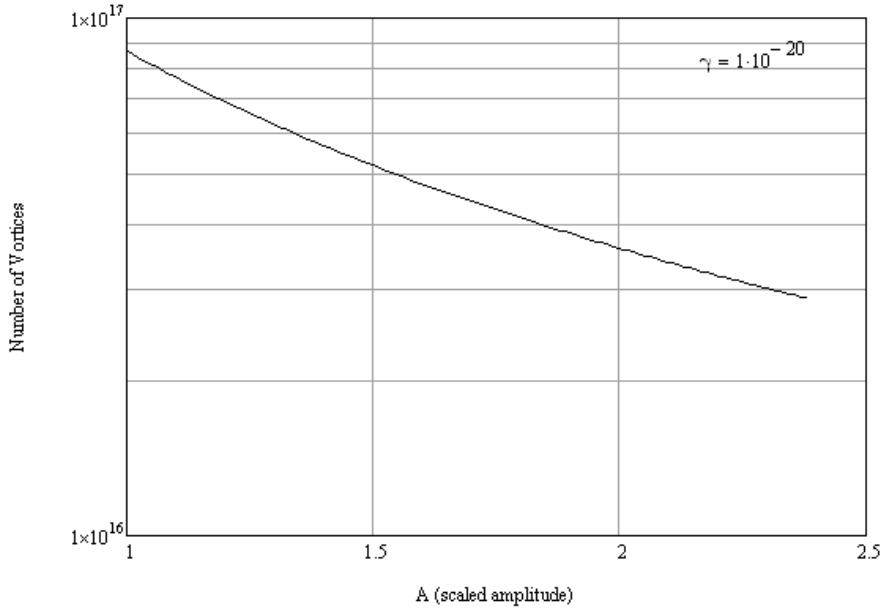

Figure 2.17: Graph of the number of vortices in the cell derived from experimental data and the viscous model with a freely determined γ on a semi-logarithmic scale.

What is quickly realized if one adjusts the value of γ is that there is no noticeable variation in the number of vortices curve between $\gamma = 1 \times 10^{-20}$ and $\gamma = 0$, so in order to find a relatively constant and reasonable number of vortices involved in the dissipation there must be in essence no dissipative force, which would result in no anomaly in the freedecays. This fact casts great doubt upon an explanation for the "kink-like" freedecays from a force that relies upon a simple proportionality with the velocity.

2.5 Summation

As was made clear in the section on the friction model, the theories advanced thus far for the additional dissipation seen in anomalous free decays are unable to completely fit the experimental data that has been seen. The "mutual friction" based model requires numbers of vortices that are impossibly large to obtain the needed dissipations and hence must be discarded.

For the friction model, there is some fundamental element of the physics missing. This is seen in its inability to fit the experimental data sets and evidence of a wildly shifting number of vortices when modeling the dissipation based on the models alone.

The introduction of a creation energy term, possibly tied to vortex ring nucleation in pockets of bulk fluid, helps to maintain a better constancy of vortices in the system. It also allows one to conclude that the dissipations are due to a rather small number of vortices (approximately three for a typical bulging nonlinear free decay) created at defects as opposed to de-pinned from them (hence

the need for the creation energy $u_\circ$.) This is a valuable conclusion as the number of participating vortices was not previously known.

Chapter 3

Vortex Positions

3.1 Introduction

In the previous chapter a conclusion was reached that there are a small number of vortices taking part in the dissipative process. That conclusion is supported in this chapter, and further, the vortex positions within the cell are examined. Note that this represents a reversal from the previous 1991 paper of Ellis and Luo. They predicted that pinned vortex densities of $10^3/\,\mathrm{cm}^3$ to $10^5/\,\mathrm{cm}^3$ would be required to produce anomalous decays of the type seen. [6]

This verification was made via a calculation of the critical velocities for each vortex of an arbitrary array of vortices placed within the experimental cell. The observed free decays will be shown to be inconsistent with a uniform distribution and the vortices will be found to be constrained to a small number of defect sites (probably one) within the cell. This is closely tied to the geometry of the resonant modes within the cell and hence a brief consideration of these is necessary

to proceed.

3.2 Resonator Modes

We must keep in mind that third sound waves are little more than shallow water waves driven in superfluid helium. As a result, they display normal modes, dictated by specific resonant frequencies ω which correspond to wave numbers k. Due to the circular nature of the resonating cavities of the third sound oscillators, the derivation of these modes can be somewhat complex. There is no need, however, to go through the full derivation of the resonator normal modes in order to grasp the significance of the modes and their importance to the determination of the positioning and number of vortices in the experimental cell. A qualitative understanding will suffice for the reader to grasp the procedure employed.

The third sound resonators from which this data was taken consisted of two glass microscope slides separated by a distance of typically 10 millimeters. A circular cavity was created between the two slides by the wicking of epoxy adhesive into the gap until the cavity was of a specific radius a, typically between 6.05 and 6.15 millimeters depending on the particular experimental cell.

The structure of the modes in these cells is dictated by Bessel functions of the first kind, J_m. These Bessel functions are the solutions to one of the third sound equations of motion:

$$\nabla^2\eta + k^2\eta = 0 \tag{3.1}$$

The n^{th} root of the derivative with respect to x of the m^{th} Bessel function is given

by the value χ_{mn}, such that:

$$\frac{d}{dx} J_m(\chi_{mn}) = 0 \tag{3.2}$$

where $(m,\ n)$ are positive integers dictating the quantization of the modes. These derivative zeros are required to impose a boundary condition, namely that the waves from the top and bottom of the resonator cavity must have the same derivative at their junction, that is $d\eta/dr = 0$ at $r = a$ (the resonator radius.) Applying this boundary condition defines our wave number k:

$$k = \chi_{mn}/a \tag{3.3}$$

There are several constants required for the eventual expression of the mode structure. The density of ^{4}He is designated as ρ and equals $145\,\mathrm{kg/\,m^3}$. The static thickness of the film, $h_\circ$, is determined by the experimental parameters of the particular film of interest and typically ranges from 2 to 7 nm. The third sound speed, c_3, is also determined by experimental parameters and typically ranges from 5 to $20\,\mathrm{m/\,s}$. The mode amplitude, η, is dependent on the driving force and is on the order of 1 Å. The dispersion relation is linear, given by $\omega = c_3 k$. The van der Waals acceleration is given by g.

Now, all that remains to find the structure of these third sound resonator modes is to solve (along with boundary conditions) the third sound equations of motion, the following set of coupled equations:

$$\nabla^2\eta + k^2\eta = 0 \tag{3.4}$$

$$\frac{d\mathbf{v}}{dt} = -g\nabla\eta \tag{3.5}$$

As in most wave systems, the third sound waves come in two varieties: standing and traveling. All of the anomalous free decays studied were of the standing wave variety, as was determined via a mode splitting analysis, so these will be the ones examined in this study. [5] Keeping in mind that these third sound waves are two-dimensional flows, the velocity field is expressed in polar coordinates and is given by:

$$\begin{bmatrix} v_r \\ v_\phi \end{bmatrix} = c_3 \frac{\eta}{h_\circ} \begin{bmatrix} -\frac{1}{k}\frac{d}{dr}\left[J_m(kr)\right]\cos(m\phi) \\ \frac{m}{kr}J_m(kr)\sin(m\phi) \end{bmatrix} \sin(\omega t) \tag{3.6}$$

3.3 Theoretical Distributions

Allow us to picture a third sound resonator of the type described with many vortices distributed throughout its film. A third sound wave is induced in the superfluid by a driving force (in the case of the experimental system electrostatically.) The driving force is turned off and a free decay of the wave begins. As this decay progresses, the vortices eventually reach some critical velocity at which some process occurs which changes the dissipation factor. The wave in the third sound resonator is not that of a one-dimensional plane wave, however. It is dictated by Equation 3.6. So, assuming all the vortices share the same critical velocity, not all of them will reach it at the same point. For the transition from super-critical to sub-critical flow to be abrupt, as was seen in the anomalous free decays, they must all reach the critical velocity within a narrowly defined window. A methodology was developed to test whether it was possible to have this small spread of critical

velocities with a large number of vortices uniformly distributed within the cell.

We begin with a theoretical distribution of vortex positions. A pseudo-random number generator creates a matrix of 1000 x and y positions within a square with side length a, the disk radius. The (x, y) pairs that fall outside of a circle of radius a are discarded, leaving a circle with a uniformly distributed array of vortex positions. These (x ,y) coordinates are then expressed in polar coordinates to allow the easy application of the velocity field functions. Figure 3.1 shows a typical distribution of a random vortex array within the cell.

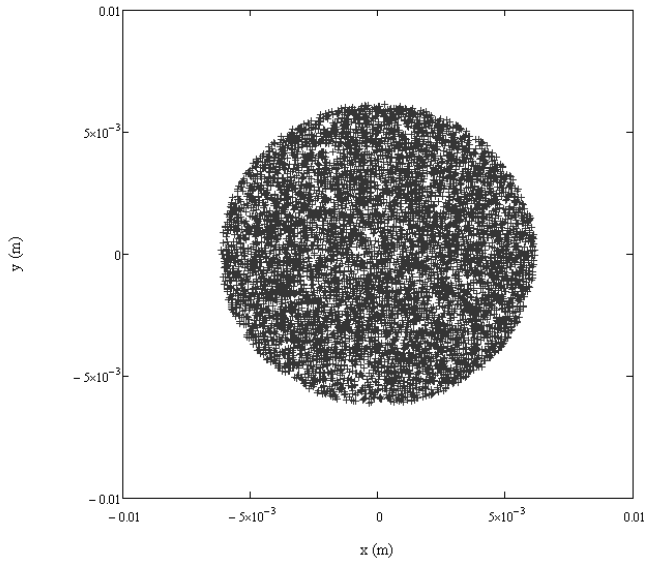

Figure 3.1: The random vortex distribution used to simulate the behavior of critical velocities across the cell.

The time dependence of the velocity equation (Equation 3.6) can be easily eliminated by restricting ourselves to the maximum of the wave structure, that is where $\sin(\omega t) = 1$ ($\omega t = \pi/2$.) In doing this, we assume the distribution of

peak velocities will reflect the distribution of critical velocities to be applied to the plane-wave result. The magnitude of the velocity field at a point is then easily found via the simple Euclidean distance formula:

$$|v_{peak}(r,\phi)| = c_3 \frac{\eta}{h_\circ} \sqrt{\left[-\frac{1}{k}\frac{d}{dr}\left[J_m(kr)\right]\cos(m\phi)\right]^2 + \left[\frac{m}{kr}J_m(kr)\sin(m\phi)\right]^2} \quad (3.7)$$

Note that the prefactors $(c_3\eta)/h_\circ$ simply set the scale for the particular film parameters. Setting these factors equal to one at the critical velocity allows the peak function to be divorced from any particular experimental conditions, giving our method some broad application. In the end, the following function was applied to the distribution of vortex positions:

$$|v_{critical}(r,\phi)| = \sqrt{\left[-\frac{1}{k}\frac{d}{dr}\left[J_m(kr)\right]\cos(m\phi)\right]^2 + \left[\frac{m}{kr}J_m(kr)\sin(m\phi)\right]^2} \quad (3.8)$$

The result is a velocity for each vortex. We plot these velocities on a histogram in order to evaluate their distribution as shown in Figure 3.2. This figure displays only the first three modes, the ($m = 1$, $n = 1$), ($m = 2$, $n = 1$), ($m = 3$, $n = 1$). These modes are the most common observed within the cell and make up nearly all of the anomalous free decays. This histogram data was also calculated for the ($m = 5$, $n = 1$) mode, but the conclusions were unchanged. The ($m = 4$, $n = 1$) mode was experimentally unobservable due to the detector geometry of the experimental cell.

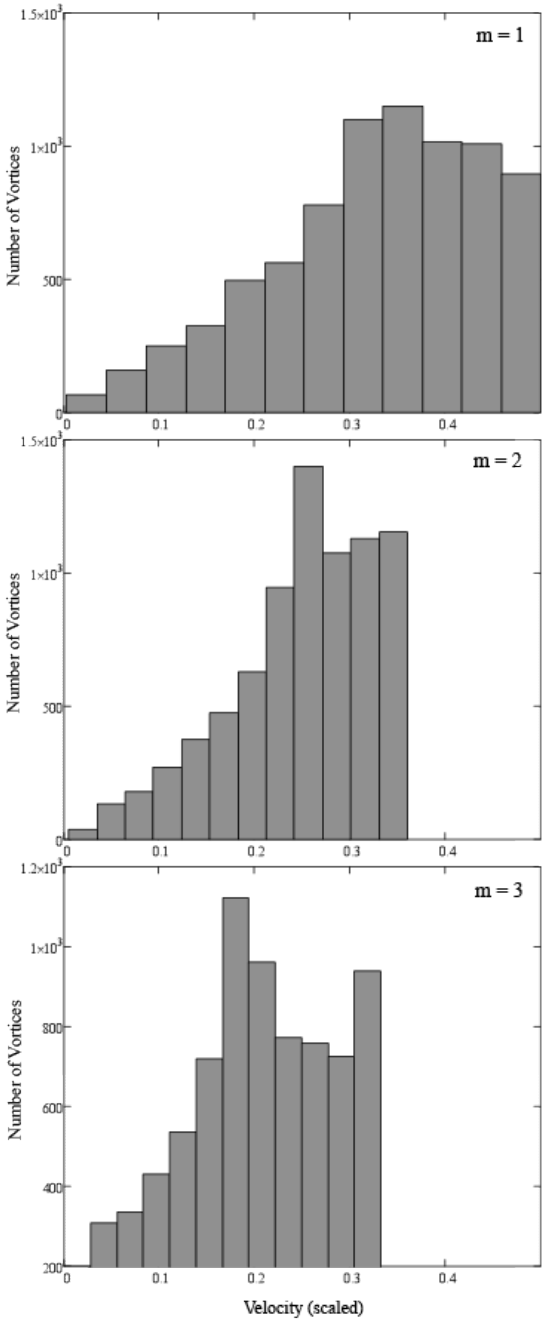

Figure 3.2: Histograms of vortex velocities for a random distribution of 10000 vortices.

In order to evaluate the physical information being displayed here, we must look at the physical structure of the mode. Figure 3.3 shows the structure of the $(m = 3, n = 1)$ mode, the most common in the experimental data. The top graph is a contour plot of the velocity field for this mode. The bottom displays the structure of the height oscillations of the mode. Note that both of these graphs are accurate qualitative representations only and are not to be taken as quantitative.

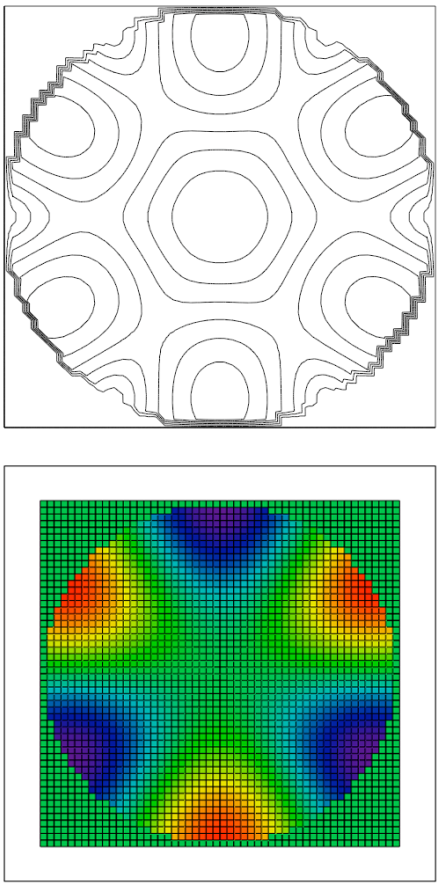

Figure 3.3: Illustration of the mode structure for $(m = 3, n = 1)$. The upper graph displays a contour plot of the velocity field and the lower displays the structure of the height oscillations of the mode.

Both these graphs clearly display the nodal structure of this mode. In the bottom graph, the height fluctuations are noted by the difference in colors. All the blue regions have the same amplitude as do the red ones for any stationary moment of the wave. In the ($m = 3$, $n = 1$) the fluid is sloshing back-and-forth between these regions throughout the wave cycle. It is logical, however, that the area of maximum flow velocity would be in between these zones. This area would correspond to the upper maxima on the graph. The other peak has a lower velocity, but a larger area, hence the larger peak.

What is important to note is that all of these curves are rather broad and while they do display maxima, the spread is still significant. As was discussed earlier, for a large number of vortices to produce an abrupt, sharp transition of the types observed, most vortices in the cell must make that transition at a similar time. This is clearly not the case for these waves: as some vortices make the transition the majority are still sub-critical. Hence, for a sharp transition to be observed, it must be the result of vortices concentrated within the same, rather narrow bands of similar flow velocity. This implies that the vortices are concentrated on a few discrete substrate defects and not scattered throughout the cell. We may predict that this small number of defect sites is probably in actuality one as it is highly unlikely (but possible) that the necessary conditions for a sharp transition described above could be met by multiple defect sites.

This data also supports the assertion of a small number of vortices involved from the previous chapter. It would be impossible to cluster a large number of vortices solely within these narrow bands. The isolated defects would quickly become saturated with vortices and lead to the annihilation of vortices with each

other. There must be a small number of vortices pinned to these isolated defects.

3.4 Summation

The analysis here supports the conclusion of the previous chapter that a small number of vortices (found to be on the order of 3) must be involved in the dissipative motion. This velocity analysis over a theoretical distribution of vortices resulted in the additional assertion that these vortices must be pinned to a few, discrete substrate defect sites lying within regions of similar velocity. We now know not only the number of vortices involved, but their physical distribution within the cell as well.

Chapter 4

Conclusion

4.1 Vortex Energies

We now return to the creation energy found in the Models chapter. We found that the creation energy of 8×10^{-19} J found in the number of vortices analysis was inconsistent with a process of vortex creation based upon the splitting of a vortex ring in a pocket of bulk fluid into a vortex/anti-vortex pair as the energies deviated by several orders of magnitude. What we now wish to do is to disregard the method of creation and look only at the energy involved with the vortices themselves.

Oliver Ryan, a member of the Quantum Fluids Laboratory, derived the energy of a superfluid film vortex in his 1992 undergraduate thesis. This derivation includes the effects of kinetic energy due to the rotating fluid, potential energy due to the van der Waals attraction with the substrate, and surface energy terms. It hence should be highly accurate and more complete than the commonly used

cylinder model.

The only inputs that are required to find an energy from this model is the film thickness h (experimentally known for each film,) and the diameter of the vortex. In order to find these diameters, we must consider that a superfluid vortex in a film will spread to encompass the maximal area possible without overlapping its neighbors. So, roughly, if we have three vortices, each will have a diameter of the radius of the cell a which for the experimental resonators with which we are concerned varies between 6.05 mm and 6.15 mm. Figure 4.1 provides an illustration of the vortices within this cell.

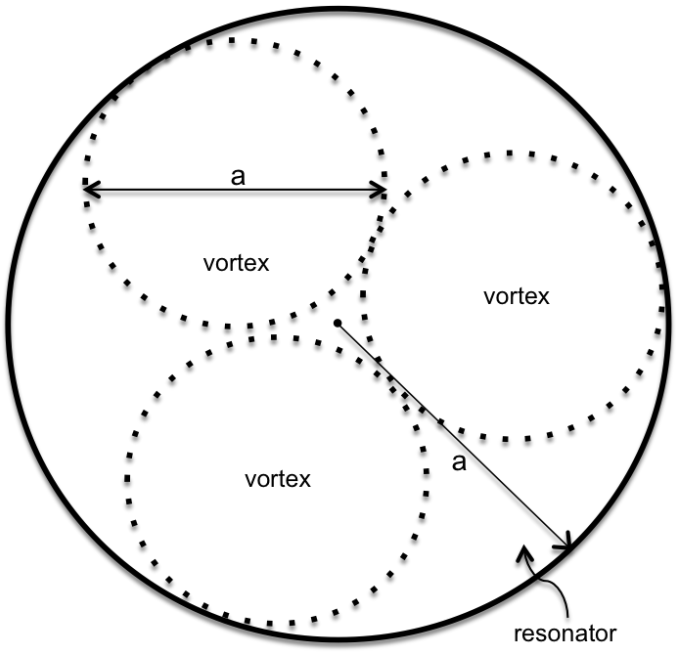

Figure 4.1: Illustration of the positioning of three vortices inside an experimental resonator cell.

Keeping this in mind, the diameter of each vortex b is approximated as:

$$b \approx \sqrt{\frac{1}{\left(\frac{\#\text{ of vortices}}{\text{cell area}}\right)}} \approx \sqrt{\frac{\pi a^2}{3}} \approx a \tag{4.1}$$

And from this we may find the energy of a single vortex from the model:

$$E_1 = \left(57\frac{\text{K}}{\text{nm}}\right)(6\,\text{nm})\ln\left(\frac{b}{1000}\right) = 4000\,\text{K} \tag{4.2}$$

So, for three vortices, we find the energy to be:

$$E_3 = 3E_1 = 12000\,\text{K} = 1.66 \times 10^{-19}\,\text{J} \tag{4.3}$$

We note that this value is 14 times smaller than the creation energy for three vortices, $3u_\circ = 2.4 \times 10^{-18}\,\text{J}$. So, we must increase the energy associated with the vortices. One option would be to increase the diameter of the vortices, but this is not feasible due to the fact that they are already at their maximal size. There is no other way to increase the energy associated with each vortex, so we must have more vortices involved in the dissipative action, but with more vortices each vortex must dissipate less. This requirement for more dissipating vortices with each dissipating less energy leads us to propose a final model for future work.

4.2 Kelvin Wave Heating Model

Superfluid vortices have the ability to transmit oscillations up and down their cylindrical cores. These take the form of helical deformations of the vortex lines

that make up the core of the vortex. [2] First written about by Lord Kelvin in 1880, these Kelvin Waves result in the loosening of pinned vortices at a lower force than is required in their absence. This phenomenon has been directly observed in bulk ^{4}He and hence should be expected to also be observed in thin films. [8] In this model the vortices exhibit two critical velocities as shown in Figure 4.2. They are initially created at a critical velocity on the order of $v_{cc} = 1\frac{\mathrm{m}}{\mathrm{s}}$. They then drag upon substrate defects as in the previous friction model. This dragging, however, pumps Kelvin Waves up the core of the vortex, in essence heating them. These heated vortices would exhibit a critical velocity on the order of $v_{ch} = 0.01\frac{\mathrm{m}}{\mathrm{s}}$ and the drag due to their friction-like pinning and depinning force would be greatly reduced. This is in keeping with the experimental data showing decreased pinning in bulk vortices with Kelvin Waves present.

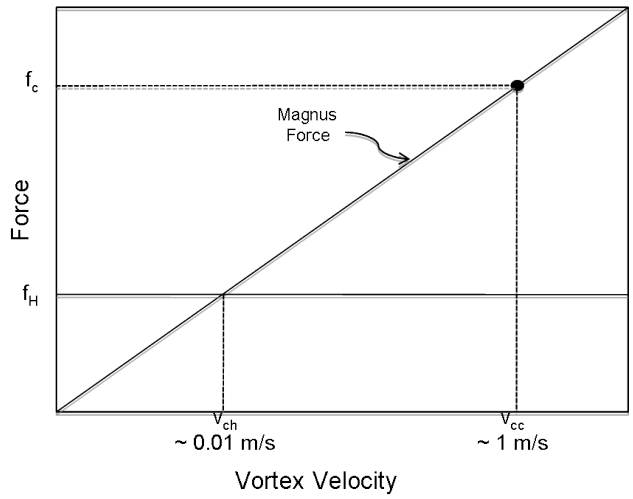

Figure 4.2: Illustration of the drag force vs. vortex velocity for the Kelvin Wave model.

This model appears to reconcile an ongoing issue with the previous models. Our freedecays clearly exhibit critical velocities on the order of $0.01\frac{\mathrm{m}}{\mathrm{s}}$. The bulk of work on critical velocities (outside the context of freedecays) in superfluid films exhibit critical velocities on the order of $1\frac{\mathrm{m}}{\mathrm{s}}$. This model would seem to hold the promise of reconciling these discrepancies and appears to be the most promising path forward for future work on these superfluid vortices.

4.3 Conclusion

This thesis set out to test the compatibility of vortex drag dissipation with the observed anomalous freedecay features. The preceding work has resulted in several new conclusions about these anomalous freedecays. First, it is clear that all of the anomalous freedecays recorded take place in standing-wave modes.

Second, the friction-based vortex pinning/depinning model fails to completely explain the observed "bulge-like" anomalous decays. The introduction of an additional dissipation in the form of a creation energy term allows us to conclude (motivated by our desire to not have many more vortices dissipating at lower amplitude) that only a small number of vortices, on the order of three, are involved in the dissipative process based on this modified model.

Third, the mutual friction-based model for the "kink-like" anomalous freedecays is not a possible explanation, due to the impossibly large numbers of vortices it predicts. In addition, it introduces a temperature dependence which was not observed in the experimental data.

Fourth, this small number of vortices must be concentrated on a very small

number of defect sites due to the structure of the resonant modes of the third sound apparatus in order to obtain the observed behavior. We may further predict that there is probably only one defect site on which these vortices are located.

Finally, it was determined that the creation energy found from the friction model was too small for the number of vortices predicted and hence the Kelvin wave heating model was proposed. This new model should provide fodder for future work on this topic and appears to hold the promise of reconciling several long-term discrepancies observed in third sound dissipation.

All of the models discussed in this work are based upon extensions of observed vortex phenomena in bulk superfluid. What will be needed going forward in the study of these anomalous freedecays and the physical mechanisms behind them are experimental studies of the same sort as have been performed in bulk superfluid helium upon vortices within the adsorbed films. This experimental verification will likely prove to be crucial in the eventual full explanation of the observed freedecay behavior and the proving or disproving of any model, including the final Kelvin wave heating model proposed above.

Bibliography

[1] David R. Tilley and John Tilley. *Superfluidity and Superconductivity*. Halsted Press, New York, 1974.

[2] Russell J. Donnelly. *Quantized vortices in helium II*. Cambridge Studies in Low Temperature Physics. Cambridge University Press, Cambridge, 1991.

[3] Ian Carbone. *Steady State and Transient Third Sound Behavior*. Undergraduate thesis, Wesleyan University, Middletown, CT, 2006.

[4] K.W. Schwarz. "Three-dimensional vortex dynamics in superfluid ^{4}He: Line-line and line-boundary interactions". *Physics Review B*, 31:5782–5804, 1985.

[5] Hai Luo. *Third Sound Resonance Detection of Superfluid Circulation*. Ph.d. thesis, Wesleyan University, Middletown, CT, 1992.

[6] F.M. Ellis and H. Luo. "Low Temperature Exponential and Linear Free Decay of Third Sound Resonances". *Physica B*, 169:521–522, 1991.

[7] Mark Andrew Carnahan. *Vortex Pair Excitations in Liquid Helium Films*. Undergraduate thesis, Wesleyan University, Middletown, CT, 1997.

[8] L. Hough L.A.K. Donev and R.J. Zieve. "Depinning of a superfluid vortex line by Kelvin waves". *Physics Review B*, 64:180512–180516, 2001.